Multi-species impurity granule injection and mass deposition projections in NSTX-U discharges

IOP Publishing | International Atomic Energy Agency Nuclear Fusion
Nucl. Fusion **57** (2017) 076008 (8pp) https://doi.org/10.1088/1741-4326/aa6cd3

Multi-species impurity granule injection and mass deposition projections in NSTX-U discharges

R. Lunsford, A. Bortolon, A.L. Roquemore, D.K. Mansfield, M.A. Jaworski, R. Kaita, R. Maingi and A. Nagy

Princeton Plasma Physics Laboratory, PO Box 451, Princeton, NJ 08543, United States of America

E-mail: rlunsfor@pppl.gov

Received 5 January 2017, revised 17 March 2017
Accepted for publication 12 April 2017
Published 16 May 2017

Abstract

By employing a neutral gas shielding (NGS) model to characterize impurity granule injection, the ablation rates for three different species of granule: lithium, boron, and carbon, are determined. Utilizing the duration of ablation events recorded on experiments performed at DIII-D to calibrate the NGS model, we quantify the ablation rate with respect to the plasma density profile. The species-specific granule shielding constant is then used to model granule ablation within NSTX-U discharges. Simulations of 300, 500 and 700 micron diameter granules injected at 50 m s^{-1} are presented for NSTX-U L-mode type plasmas, as well as H-mode discharges with low natural ELM frequency. Additionally, ablation calculations of 500 micron granules of each species are presented at velocities ranging from 50–150 m s^{-1}. In H-mode discharges these simulations show that the majority of the injected granule is ablated within or just past the edge steep gradient region. At this radial position, the perturbation to the background plasma generated by the ablating granule can lead to conditions advantageous for the rapid triggering of ELM crashes.

Keywords: granule injection, ELM pacing, neutral gas shielding

(Some figures may appear in colour only in the online journal)

1. Introduction

The ability to control edge localized modes (ELMs) is required for successful operation of next generation plasma devices such as ITER. For discharges with a naturally low ELM frequency, on the order of a few Hertz, the impurity ejection provided by spontaneously occurring ELMs is projected to be insufficient to control core impurity buildup. To maintain a low Z_{eff}, the period between the ELMs must be smaller than the edge to core transport times of the sputtered divertor and first wall material. During the hydrogen/helium operational phase of ITER, the intrinsic ELM frequency is anticipated to be too low to provide sufficient impurity exhaust, and must be augmented through one or more techniques [1, 2]. In addition the impact of unmitigated ELMs can lead to localized melting which can give rise to injected W droplets, resulting in a radiative collapse of the discharge or triggering a disruption [3, 4]. As the plasma current is increased, the spatial footprint of the energy exhausted to the plasma-facing components (PFCs) by ELMs narrows and the unmitigated peak heat flux can exceed material integrity limits. To ameliorate this effect, previous experiments [5] have demonstrated that, in certain circumstances, there is an inverse relationship between the frequency of the triggered ELM and the peak heat flux contained within the mode. Thus to generate the required mitigation, a rapid triggering of ELMs is employed to reduce the peak heat flux. While recent results have called into question the efficacy of pellet pacing in metal walled tokamaks [6, 7], ELM triggering through pellet pacing and 3D edge magnetic field perturbations [8] remain the baseline ELM heat flux mitigation strategies envisioned for ITER.

The injection of deuterium pellets into the edge of a magnetically confined plasma is one of the methods used to generate on-demand triggering of ELMs through the seeding of

a torodially localized pressure perturbations. Pellets injected into the discharge are rapidly heated by background plasma electrons traversing field lines. The surface of the pellet ablates and forms a dense neutral cloud, shielding the solid body from further direct heating. The effect of this neutral gas shielding (NGS) [9] is to reduce the thermal flux to the solid core. Additional heating ionizes the neutral cloud which is then primarily transported away along field lines at the ion thermal speed, this continues until the supporting pellet is consumed. Non-linear modelling of the resultant pressure perturbation has been carried out [10] and demonstrates that if the rise in local plasma pressure is sufficient, then the over-dense flux tube can exhibit a ballooning-type instability, thus resulting in a triggered ELM [11]. These stimulated ELMs can display an inverse relationship between the pellet injection frequency and the resultant peak heat flux, reducing the efflux of particles and energy to a level tractable for the PFCs [12].

ELM triggering can also be accomplished by injection of non-fueling impurity granules. At DIII-D the injection of sub-millimeter lithium granules has been shown to trigger and pace ELMs [13]. Granules ranging in diameter from 300 to 900 microns were injected at velocities between 50–120 m s^{-1}. The ELM triggering efficiency was found to depend heavily upon the granule size, with the smaller granules only triggering ELMs approximately 30% of the time, while the injection of granules larger 900 microns resulted in the prompt triggering of an ELM nearly 100% of the time. In addition, ELM pacing at a rate of 3–5 times the natural ELM frequency was observed and has been shown to produce a similar heat flux mitigation effect under certain conditions. In further experiments at DIII-D, described here, in addition to lithium, the injection of both carbon and boron carbide granules have also been shown to trigger ELMs. In recent experiments at ASDEX Upgrade [14] cylindrical lithium pellets 1.5 mm in diameter by 2.0 mm in height were injected at 585 m s^{-1} at a frequency of 2 Hz. While this injection frequency was too slow to achieve pacing, ELM triggering was observed in a majority of the cases. When an injected pellet failed to trigger an ELM, it is unknown at this time if this was due to the enhanced speed of the pellet when compared to the DIII-D case, as this leads to a deeper penetration of the impurity source and a reduced pedestal localized pressure perturbation, or if it is a consequence of the metal wall induced ELM trigger lag phenomenon which has been observed with deuterium pellet pacing on JET [6] and AUG [7].

The granule injector first employed at EAST [15], followed by versions on DIII-D and NSTX-U utilizes a dual-bladed rotating impeller made from a thermoplastic polymer driven at rotation frequencies of up to 250 Hz, allowing for pacing frequencies of up to 500 Hz and injection velocities of up to 150 m s^{-1}. This impeller redirects gravitationally accelerated solid impurity micro-granules horizontally into the low field side of the discharge, near the outer midplane.

Utilizing the granule injection experiments at DIII-D we calibrate an NGS model [16] for granule ablation to determine a species-specific granule shielding parameter. This model calculates the fractional portion of the granule mass deposited at the top of the pedestal. It is believed that this metric is directly correlated to the probability that the injected granule will trigger an ELM. When applied to NSTX-U H-Mode discharges, for a granule injector operating at a mid-range injection velocity of 100 m s^{-1}, the NGS simulation projects that an ablating granule will deliver nominal central mass deposition distances of approximately 3 cm and 8 cm for 500 micron lithium and carbon granules respectively. Reducing the impeller frequency ameliorates the impurity influx to the discharge core by an outward shift in the depositional barycenter, allowing the injected mass to remain closer to the separatrix, where up to 80% of the granule material is promptly flushed by the stimulated ELM [17].

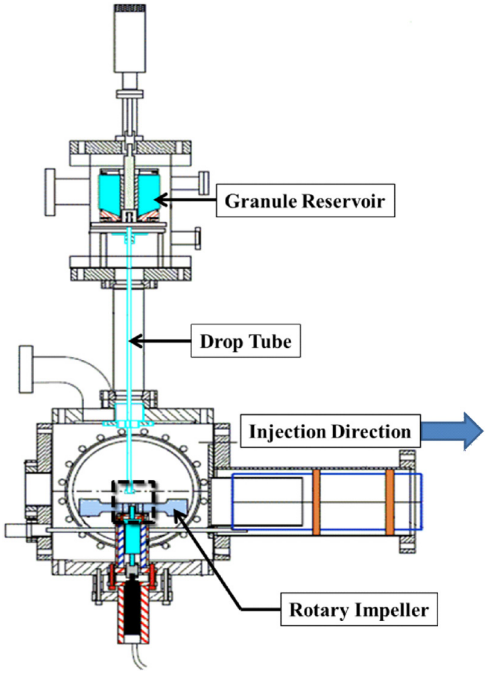

Figure 1. Granule injector cutaway. Granules travel from the reservoir, down the drop tube and are driven into the discharge by the impeller. The dashed black box denotes the region of interest for the photograph series in figure 2.

The remainder of this paper discusses the granule injector apparatus, details the granule ablation model, and then extrapolates the results of these injection characteristics in NSTX-U discharges by utilizing the experiments at DIII-D as a benchmark.

2. Experimental set-up

The impurity granule injector (IGI) was designed at PPPL and first deployed for lithium granule injection experiments on the EAST tokomak. As is shown in figure 1, the granules are housed in a reservoir positioned above the injection chamber. A vibrating piezoelectric disk at the bottom of the reservoir is driven at a resonance of 2250 Hz. This frequency generates a node at the center of the disk, driving the granules toward a circular aperture located above the drop tube. Granules fall into the drop tube where they are gravitationally accelerated. At the end of the tube, a rapidly rotating dual-bladed turbine

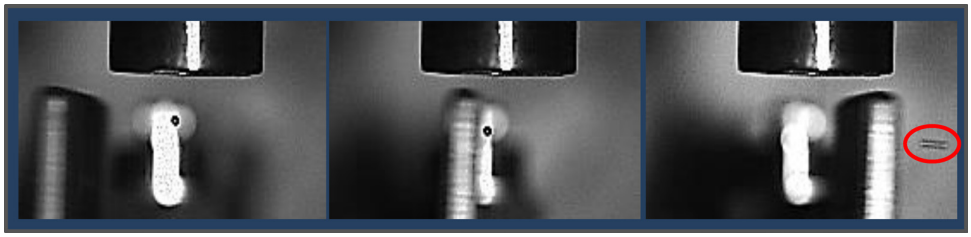

Figure 2. Horizontal injection of a 700 micron carbon microsphere. Exposure time is 50 μs and inter-frame time is 200 μs. Motion blur of the rightmost granule (circled) gives an estimated velocity of 45 m s^{-1}.

impeller redirects the granules into the edge of the discharge as shown in figure 2. By adjusting the driving voltage to the piezoelectric disk, the granule drop frequency can be roughly controlled. Likewise, by altering the rotation speed of the impeller, the granule injection speed and maximum injection frequency can be adjusted. Granule drop frequencies can be varied from a single granule injection up to approximately 300 Hz. Injection velocities can range from 40–100 m s^{-1} for malleable granules such a lithium, and from 40–150 m s^{-1} for rigid granules, such as vitreous carbon. This variation is due to deformation observed during paddle impact with the more ductile species of granule. Velocities below 40 m s^{-1} are impractical due to substantial parabolic decay of the trajectory during horizontal injections. The dropper and impeller method of granule delivery provides a simple and robust method of injection at a range of frequencies, granule sizes (100–1000 micron diameters) and velocities. Note however that the dropper disk and the impeller are uncoupled, leading to an asynchronous delivery of granules. Further details about the system can be found in [18, 19].

The granules to be injected have been acquired from a variety of sources. Lithium granules have been supplied by FMC Lithium (www.fmclithium.com) and are 99.9% pure Li by weight. A typical assay of additional impurity contents has been provided by FMC Lithium and shows the primary additional impurity to be nitrogen at a level of 300 parts per million by weight. The carbon microspheres utilized in these experiments are supplied by Alfa Aesar (www.alfa.com) and are a formulation known as vitreous carbon. Vitreous carbon, also known as glassy carbon, is distinct from the nominal graphitizing carbon by its low density, extreme hardness and chemical resistivity. These qualities are a direct result of its unique structure. An examination of high resolution transmission electron microscopy (HRTEM) images of vitreous carbon display tightly curled graphene planes encircling nanometer scale micropores in a conglomeration of fullerene related structures [20]. These properties result in highly uniform microspheres which flow easily, without the dust generation resultant for graphitic carbon. The high purity boron carbide granules are provided by Industrial Supply Inc. (www.sandblastingabrasives.com), and, unlike the lithium or carbon microspheres, are irregularly shaped. This irregularity results in a larger injection cone when the granules are impacted by the impeller, and thus a lower injection fraction as defined as the ratio of granules dropped to granules which are injected into the discharge. The boron carbide (B_4C) compound is a complex 12 atom icosahedral form arrayed in a rhombohedral

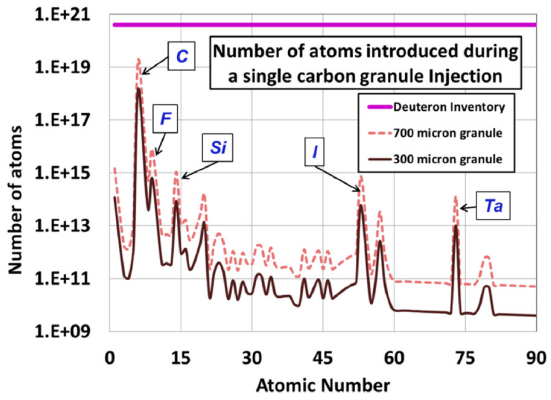

Figure 3. Impurity load from carbon granule injection. Relative abundances of primary and secondary impurities are displayed along with an elemental identification of the largest contributors as compared to a nominal NSTX deuteron inventory.

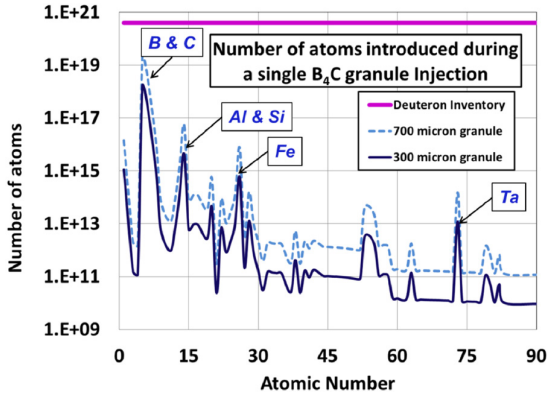

Figure 4. Impurity load from boron carbide granule injection. Relative abundances of primary and secondary impurities are displayed along with an elemental identification of the largest contributors as compared to a nominal NSTX deuteron inventory.

lattice [21]. This arrangement creates a compound that exhibits extreme hardness at low density, along with thermal stability and a high melting point. This granule species was chosen to be compatible with devices with carbon PFCs that employ boronization as a wall conditioning technique.

To determine the additional impurity content of the carbon and boron carbide granules, samples were sent to the Evans Analytical Group Laboratories (www.eag.com) for detailed elemental analysis utilizing plasma desorption spectroscopy. The results of this analysis is shown in figures 3 and 4, which display the typical granule induced impurity load, both main

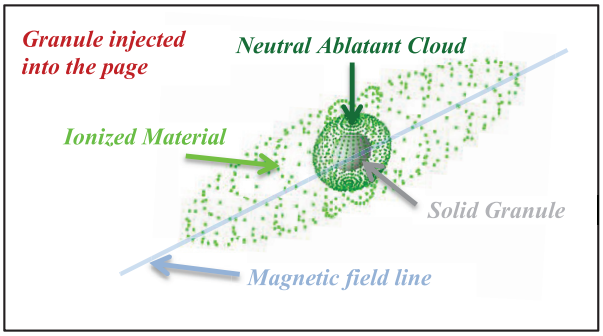

Figure 5. Ablation characteristics of an injected solid granule.

species and trace impurity, for a nominal single granule injection at both 300 and 700 micron granule diameters. The deuteron inventory for a typical NSTX discharge is also displayed for reference [22].

3. NGS model of granule ablation

Upon injection of a granule into the low field side of a fusion research plasma, electron heat conduction along the magnetic field lines causes the outer layer of the granule to rapidly ablate. As shown in figure 5, the ablatant forms a dense neutral cloud, partially shielding the granule from the surrounding plasma. Further heat input to the neutral cloud results in an ionization of the ablatant material, which is then conducted away from the granule along field lines at the ion acoustic speed. This quasi-stasis of granule and neutral cloud is maintained until the granule can no longer replace the ablatant material lost to ionization. Observations of injected granules confirm the overall cigar shape of the ablation cloud [23], and the occultation of the injected granule during injection is indicative of the described dense neutral cloud. The prompt mass deposition of these granules into the edge of the discharge leads to a peaking of the localized plasma pressure and the creation of an overdense flux tube, which in turn becomes 3D ballooning unstable, resulting in an ELM.

Following [9, 24] the ablation rate (G) of the injected granule is given by equation (1)

$$G = 4\pi q_s \eta \xi_g f_B \tag{1}$$

where f_B is the combined field-directed anisotropy and flux screening parameter, and is numerically equal to 0.08 [16]; q_s is the heat flux variable as described by equation (2)

$$q_s = \frac{1}{2} n_e T_e \left(\frac{8T_e}{\pi m_e}\right)^{1/2} \tag{2}$$

with the nominal definitions of the plasma parameters n_e, T_e, and m_e. The characteristic granule parameter (ξ_g) is given by equation (3)

$$\xi_g = \frac{r_g^2}{n_g}\left[\Delta H + \frac{10}{3}T_s\right]^{-1} \tag{3}$$

and is comprised of the granule radius (r_g), the solid granule density (n_g), the sublimation energy of the granule (ΔH) and the surface temperature of the ablating granule (T_s). For these calculations the surface temperature is assumed to be either the boiling point, or the vaporization temperature of the granule material. The density, sublimation energy, and surface temperature of the candidate granule materials, as well as the estimated number of electrons per injected granule, are summarized in table 1. Finally the cloud shielding parameter (η), as defined in [16], represents the fractional efficiency of the neutral-ablated material in shielding the solid granule from the incoming electron flux. The shielding parameter characterizes the ratio of the energy (E) which reaches the surface of the granule as compared to the thermal reservoir of the flux tube (E_g/E_∞). For deuterium pellets, the low sublimation energy ($\Delta H_D = 0.0155$ eV/atom) of the slush pellet results in a dense neutral cloud that almost fully shields the pellet, thus attenuation of the heat flux is substantial and the energy reaching the surface is nearly zero ($E_g/E_\infty \sim 0$). For solid impurity granules, the sublimation energy is at least 2 orders of magnitude higher, resulting in only partial shielding of the granule. In high z granules η approaches unity which indicated that the granule transverses the plasma essentially unshielded. This parameter is experimentally determined as described in the following section and also listed in table 1.

4. Determination of granule shielding parameter from DIII-D ITER baseline injection experiments

A calibration of the NGS model described in the previous section was performed during granule injection experiments on DIII-D [25]. A high-speed camera located at the back of the IGI system and optically aligned radially inward along the injection vector was used to observe the ionization emission from the injected granules. By fitting the time envelope of the ablation event to the calculation of the granule lifetime, the cloud shielding parameter η was experimentally determined. It was then utilized to ascertain a decay rate for the injected granule radius, thus resulting in a mass deposition rate within the plasma and consequently a penetration depth of the solid granule.

Subsequent experiments were performed on DIII-D utilizing multi-species impurity granule injection [26] into low torque ITER baseline discharges. The resultant ablation times for the various granules are displayed in figure 6. A comparison of the ablation times for similar sized granules injected into roughly equivalent discharges showed an ablation rate that was accelerated by approximately a factor of 1.7 in these low torque discharges. This factor is the result of the IGI granule flight path being located geometrically close and roughly perpendicular to the trajectory of the counter propagating neutral beam, which was utilized to heat the ITER baseline discharge [27]. The ability of an incident energy source to accelerate the ablation process of injected pellets has been documented in the literature [28], and was observed in these experiments by noting that the lithium granules began to evaporate as soon as they had traversed the tile shadow, prior to any contact with the last closed flux surface (LCFS) [29]. We thus adopt the 0.3 granule shielding factor ascribed to lithium granule ablation during the initial

Table 1. Granule composition factors. The table lists species-specific granule factors used in the ablation calculation. Note that the granule shielding parameter listed for boron was arrived at utilizing boron carbide granule injections.

	Density (atoms m^{-3})	Sublimation energy (eV/atom)	Granule surface temperature (eV)	Number of electrons/500 micron granule	Granule shielding parameter
Lithium	4.6×10^{28}	1.6	0.14	9.1×10^{18}	0.3 ± 0.1
Boron	1.3×10^{29}	5.3	0.36	5.2×10^{19}	0.7 ± 0.3
Carbon	1.12×10^{29}	7.5	0.34	4.2×10^{19}	0.4 ± 0.2

granule injection experiments [25]. We then utilize the neutral beam ablation enhancement factor of 1.7 to renormalize the granule shielding factors for injected carbon and boron carbide granules recorded during the DIII-D experiments into a self-consistent basis set of granule shielding factors relevant to the high torque discharges expected in NSTX-U. The carbon granule neutral shielding factor was determined to be 0.4, which is consistent with the range of values described in [16]. The granule shielding factor for boron carbide was found to be substantially higher at 0.7. This result indicates that the granule was less effective at generating a shielding neutral cloud, and thus ablated more rapidly than is expected by comparing the inherent material properties between boron and carbon. However we note that this ablation picture is incomplete as the boron carbide granules were irregularly shaped, possibly leading to both a greater variation in total mass for the sifted granules as well as an accelerated localized heating of sharp granule edges. These factors are evident in the larger variations in ablation time observed for this species of granule. In addition, a substantial fraction of the injected boron carbide granules fractured during encroachment into the steep gradient region, which we postulate may be due to thermal stresses on the crystallographic structure planes of the boron carbide construct. Further exploration of these effects will be the focus of future work.

5. Numerical simulation of granule injections into NSTX-U discharges

The experimentally obtained species specific values for the cloud shielding parameter were adopted for the simulation of granule injection into NSTX-U discharges, to project the ablation characteristics for three different species of granules (Li, B, C). Injection of 300, 500, and 700 micron diameter granules at 50 m s^{-1} is simulated into both an NSTX-U L-mode discharge (#204563) and an NSTX-U H-mode discharge (#204118) with low natural ELM frequency. For the purposes of these simulations the temperature and density for the L-mode were sampled at 650 ms. Plasma parameters at this time were: toroidal field (B_T) = 0.63 T, plasma current (I_P) = 640 kA, total stored energy (W_{Tot}) = 65 kJ, beta normal (β_N) ≈ 1.8, and safety factor (q_{95}) ≈ 4.8. The H-mode edge profile was also sampled at 650 ms and the resultant plasma parameters were: $B_T = 0.63$ T, $I_P = 1$ MA, $W_{Tot} = 334$ kJ, $\beta_N \approx 4.5$, and $q_{95} \approx 6.7$. The granule sizes stated above were chosen during the design phase of the granule injector to span the space most likely to trigger ELMs while generating a minimal impurity overburden to the receiving plasma. The simulation velocity represents a minimal

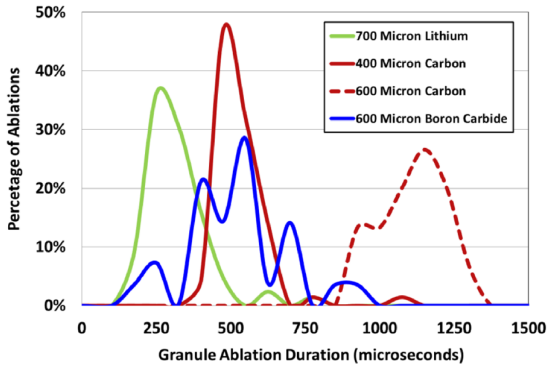

Figure 6. The duration of ablation events recorded for lithium granule injection (DIII-D #165410), two sizes of carbon granule injection (DIII-D #165406 and #165409 respectively), and boron carbide injection (DIII-D #165418).

effective injection velocity of the granule injector. It was chosen to ensure granule penetration of the discharge while resulting in the most outboard deposition of the ablated material, thus mitigating the core contamination. For figures 7–9 the darker traces are representative of granules injected into an H-mode type discharge while the lighter traces are calculations of the ablation rates in an L-mode discharge. Electron densities for the respective modes are also displayed in the solid black and gray traces. Simulated granules are injected from the larger radius on the right hand side of the graphs and ablate as they transit from right to left towards the magnetic axis of NSTX-U which is nominally located at a radius of 1.0–1.1 m depending on the discharge.

5.1. Variations in granule size and plasma parameters

In figure 7, the calculated ablation profiles of injected lithium granules into the edge of NSTX-U discharges are shown. As is shown, the ablatant deposition is strongly peaked near the pedestal edge for granule injections into H-mode, and the penetration depth of the injected granules is commensurately reduced by almost a factor of 3 when compared to injections in L-mode discharges. The strong peaking is coincident with the H-mode pedestal, as measured by Thomson scattering and shown by the black trace displayed on the figures. The lower sublimation energy for lithium, with respect to carbon and boron results in a rapid ablation of the granule as it enters the discharge. This co-location of the ablatant deposition and the steep gradient region results in a localized pressure perturbation that is beneficial for the triggering of an ELM.

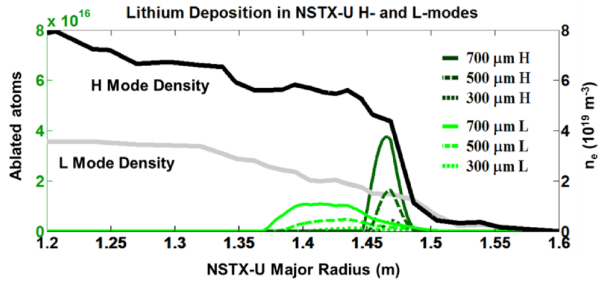

Figure 7. Simulated ablatant deposition location for various sized lithium granules injected at 50 m s^{-1} into NSTX-U H and L-modes.

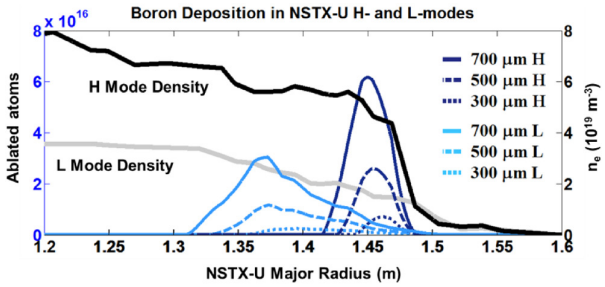

Figure 8. Simulated ablatant deposition location for various sized boron granules injected at 50 m s^{-1} into NSTX-U H and L-modes.

The ablatant deposition location for boron granules is displayed in figure 8. While experiments will be undertaken with boron carbide granules, the simulations were performed with pure boron granules for simplicity. The higher sublimation energy of boron granules results in a deeper penetration than those seen with lithium, while the higher density results in a respectively larger number of atoms introduced into the edge discharge for an injected granule of the same size, thus generating a greater density perturbation than seen with lithium.

The simulation of carbon granule injection shown in figure 9 displays a similar behavior to the boron granules. However, despite a similar density to boron, the larger sublimation energy of the carbon granule (7.5 eV versus 5.3 eV) results in an even deeper penetration and consequently an ablatant distribution that is not as strongly peaked. For the largest granule injections into L-mode type plasmas the granule does not fully ablate until it has reached ~30 cm into the discharge, even at this low injection velocity.

5.2. Variations in granule velocity

To further explore the mass deposition characteristics of injected impurity granules, we now focus primarily on the midsize (500 micron) granules and vary the injection velocity over the range available to the granule injector (40–150 m s^{-1}). Altering the injection velocity of the granule, presented in the lower three intensity graphs in figure 10, can further modify the mass deposition location, allowing tuning of the localized pressure perturbation and thus affecting the ELM triggering efficiency. By reducing the rotation speed of the impeller, the peak mass deposition location is translated closer to the top

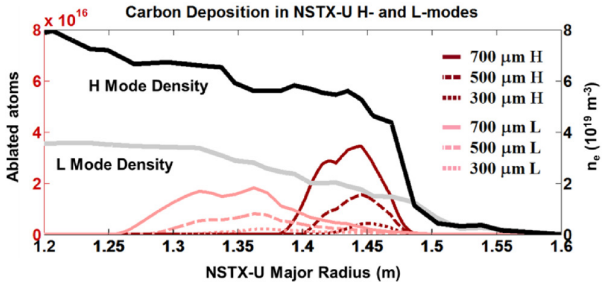

Figure 9. Simulated ablatant deposition location for 500 micron carbon granules injected at 50 m s^{-1} into NSTX-U H and L-modes.

of the pedestal. At this location the pressure profile generated by the granule can be added to the pre-existing pedestal pressure gradient, leading to a set of characteristics advantageous for ELM triggering with minimal perturbation to the core plasma. As shown in the upper panel of figure 10, variations in the depositional barycenter can range from approximately 3 cm for lithium to 8 cm for the same size (500 microns) and velocity (100 m s^{-1}) carbon granule.

Lithium granules, with their relatively low sublimation energy, are found to ablate rapidly at the edge of the discharge independent of the injection velocity. This insensitivity to velocity could explain the findings of previous experiments which reported ELM triggering efficiency to be primarily dependent upon the size of the granule [13] and the number of ablated atoms deposited atop the pedestal [25] with the injection velocity presenting minimal effect. In contrast the velocity depositional tuning effect can substantially vary the ablation profile in the boron and carbon granules. This effect may lead to a more significant injection velocity effect and should be explored in further experiments.

This calculation of the ablatant deposition location is predicated on the granule maintaining a constant velocity during injection. The possibility of a non-uniform granule ablation exists, as observed in deuterium pellet injection, whereby there is an increased ablation rate on the high field side of the granule due to the elevated heat flux. This increased ablation rate generates a so-called 'rocket effect' [23, 30] which decelerates the granule. In addition, the NGS calculations performed herein implicitly assume that the flux tube transited by the granule has sufficient energy reservoir such that the ablation process does not appreciably deplete the flux tube and that the radiative loss mechanisms have a minimal impact over the granule transit time. If the depletion of the background energy is not perturbative, then the ablation becomes self limiting [31] which leads to an enhanced granule penetration. These effects have been observed with deeply penetrating high speed lithium granules interacting with the closed central flux surfaces in AUG [14] as well as on TFTR [32]. The possibility also exists for an electric field developed by the shielding cloud to generate an $E \times B$ rotation of the shielding column which periodically ejects 'cloudlets' [33] thus reducing the shielding efficiency. This variation in the shielding is observed as a series of periodic striations in the ablation trail as the ablation rate fluctuates.

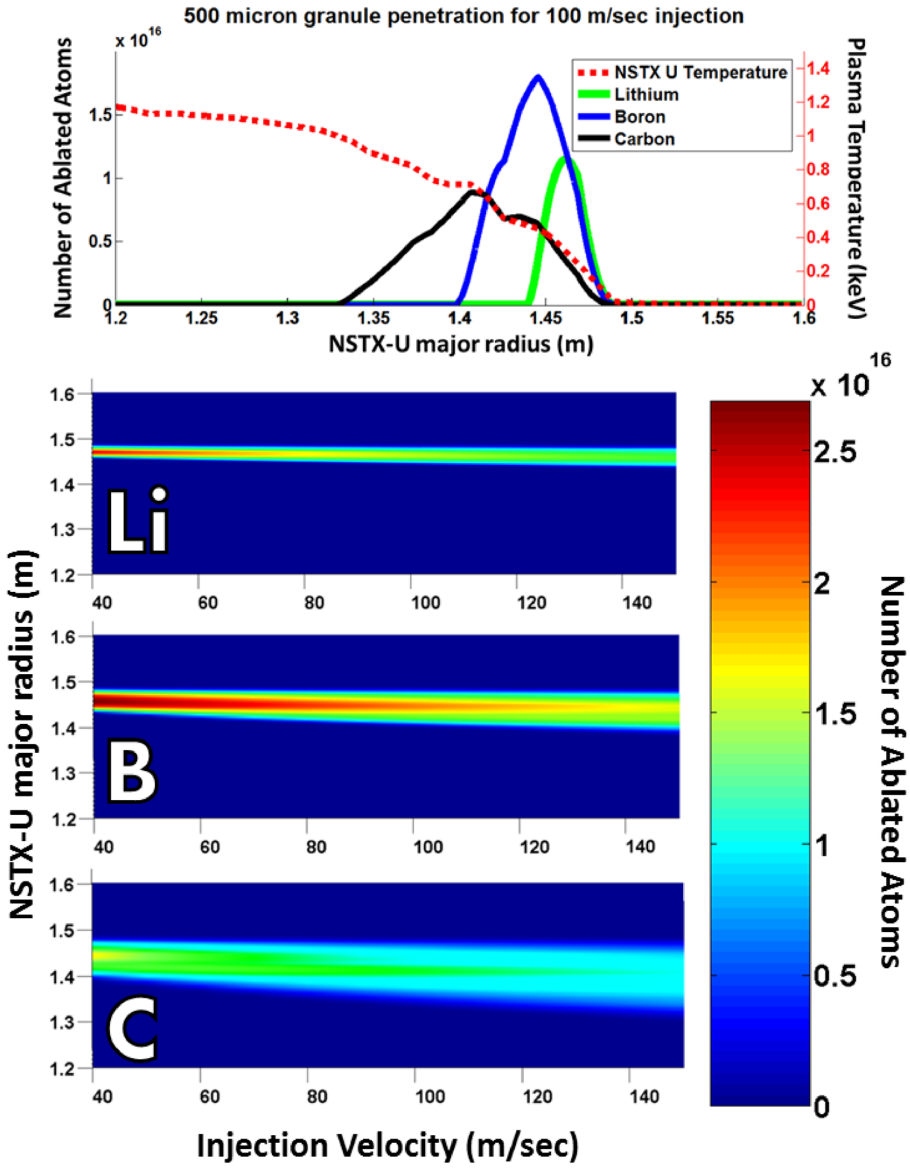

Figure 10. Mass deposition location for injected granules of differing species. The top panel displays the ablatant deposition for three 500 micron granules injected at 100 m s^{-1}. The bottom three panels illustrate the variation in mass deposition location for alternate injection velocities. In these graphs the granule injection direction is from top to bottom.

While these effects have been well documented [28] for deuterium pellet injection, further study is warranted when examining the effects on low speed impurity granules. The utilization of an extensive camera imaging and photodiode recording suite on NSTX-U will allow observation of the full injection trajectory thus permitting diagnosis of these possible effects and will contribute to further refinements of the model presented herein.

6. Conclusion

The injection of pellets or granules into the edge of a fusion research plasma has been shown to trigger ELMs through the seeding of a toroidally localized pressure perturbation that drives a region of the discharge past the peeling/ballooning stability threshold. This on-demand ELM triggering allows for fuel and impurity density control, and is an ITER baseline mechanism for ELM size mitigation through the utilization of pacing at higher than the natural ELM frequency. Triggering these ELMs through the injection of low Z impurity granules has the added benefit of decoupling the pacing mechanism from the fueling cycle, which ameliorates the pumping requirements from high speed pacing. On the other hand, impurity granule pacing does create issues of dust generation and a possible impurity overload of the discharge. To quantify these issues, further study is required.

We have utilized an NGS ablation model to characterize the injection of lithium, boron and carbon granules. The

granule shielding parameter was experimentally determined by monitoring the ablation duration for several sizes of lithium granules during their injection into DIII-D H-Mode plasmas. Adopting this parameter we are able to project the ablation rates and mass deposition profiles for multi-species granule injections on NSTX-U. The NSTX-U discharges utilized for this simulation are taken from the first operational year of the upgraded system. Looking at the NGS model (equation (2)), we estimate that these penetration depths will be reduced by a factor proportional to $q_s \sim n_e T_e^{3/2}$ as the full NSTX-U capabilities are realized. This includes increases in B_T from 0.65 T to 1.0 T, I_P from 1 MA to 2 MA, and $P_{auxiliary}$ increased from 5 MW to ~14 MW.

By adjusting granule size, composition and velocity, the edge pressure perturbation resultant from an injected granule can be tailored to the necessary requirements for ELM triggering while minimizing deleterious effects on discharge performance. Utilizing lithium, boron and carbon granules in future injection experiments facilitates the extrapolation of plasma response to the injection of beryllium granules, which is an intrinsic ITER PFC material. Extrapolation to this material then allows a benchmarking of the requirements for impurity granule pacing on next generation fusion devices such as ITER. The expansion of this model to a species-specific granule shielding parameter will be the focus of future work.

Acknowledgment

This work was supported by US Department of Energy Contract No. DE-AC02-09CH11466. The digital data for this paper can be found at http://arks.princeton.edu/ark:/88435/dsp012j62s7356.

References

[1] Evans T.E. 2013 *J. Nucl. Mater.* **438** S11–8
[2] Loarte A. *et al* 2014 *Nucl. Fusion* **54** 033007
[3] Coenen J.W. *et al* 2015 *J. Nucl. Mater.* **463** 78–84
[4] Lipschultz B. *et al* 2012 *Nucl. Fusion* **52** 123002
[5] Baylor L.R. *et al* 2013 *Phys. Rev. Lett.* **110** 245001
[6] Lang P.T. *et al* 2013 *Nucl. Fusion* **53** 073010
[7] Lang P.T. *et al* 2014 *Nucl. Fusion* **54** 083009
[8] Suttrop W. *et al* 2011 *Phys. Rev. Lett.* **109** 225004
[9] Parks P.B. *et al* 1994 *Nucl. Fusion* **34** 417
[10] Futatani S. *et al* 2014 *Nucl. Fusion* **54** 073008
[11] Huysmans G.T.A. *et al* 2009 *Plasma Phys. Control. Fusion* **51** 124012
[12] Baylor L. *et al* 2015 *J. Nucl. Mater.* **463** 104–8
[13] Bortolon A. *et al* 2016 *Nucl. Fusion* **56** 056008
[14] Lang P.T. *et al* 2017 *Nucl. Fusion* **57** 016030
[15] Mansfield D.K. *et al* 2013 *Nucl. Fusion* **53** 113023
[16] Parks P.B. *et al* 1988 *Nucl. Fusion* **28** 477
[17] Baylor L. *et al* 1999 *J. Nucl. Mater* **266–9** 457–61
[18] Roquemore A.L. *et al* 2011 *Fusion Eng. Des.* **86** 1355
[19] Mansfield D.K. *et al* 2010 *Fusion Eng. Des.* **85** 890
[20] Harris P.J.F. 2004 *Phil. Mag.* **84** 3159
[21] Domnich V. *et al* 2011 *J. Am. Ceram. Soc.* **94** 3605
[22] Scotti F. *et al* 2013 *Nucl. Fusion* **53** 083001
[23] Müller H.W. *et al* 2002 *Nucl. Fusion* **42** 301
[24] Kocsis G. *et al* 1999 *Plasma Phys. Control. Fusion* **41** 881–98
[25] Lunsford R. *et al* 2016 *Fusion Eng. Des.* **112** 621
[26] Bortolon A. *et al* 2016 Effectiveness of high-frequency ELM pacing with deuterium and non-fuel pellets in DIII-D *Preprint: 2016 IAEA Int. Conf. on Fusion Energy (Kyoto, Japan)* EX/10-1
[27] Jackson G.L. *et al* 2015 *Nucl. Fusion* **55** 023004
[28] Pégourié B. 2007 *Plasma Phys. Control. Fusion* **49** R87
[29] Bortolon A. *et al* 2016 *Bull. Am. Phys. Soc.* **61** 10.0063
[30] Moria S. *et al* 2002 *Nucl. Fusion* **42** 876
[31] Houlberg W.A. *et al* 1988 *Nucl. Fusion* **28** 595
[32] Sergeev V.Y. *et al* 1992 *Rev. Sci. Instrum.* **63** 4984
[33] Parks P.B. 1996 *Plasma Phys. Control. Fusion* **38** 571